Rotating the heading angle of underactuated flapping-wing flyers by wriggle-steering

Sawyer B. Fuller*, John P. Whitney†, and Robert J. Wood*

***Abstract*— The Harvard Robobee is a fly-sized aerial vehicle that can perform controlled flight maneuvers. But this robot is unable to control its yaw or heading angle to a desired value. Motivated by this deficiency, we propose a new method to produce yaw-axis rotations. Termed *wriggle-steering*, it consists of driving body oscillations around its two other rotational axes. Because no torque is applied directly around the controlled axis, it therefore constitutes an alternative control method for under-actuated designs. Oscillations are driven around pitch and roll axes at the same frequency but 90 degrees out of phase, resulting in a small change in yaw angle after each cycle because of nonlinearity in attitude dynamics. We propose two wing kinematics perturbations that produce the necessary actuation. The predictions are validated with a quasi-steady aerodynamics model, free-body simulations, and flight tests on a fly-sized hovering aerial robot. The results suggest that wriggle-steering can save mass and reduce complexity by eliminating the need for additional actuators in flapping-wing robots or other aircraft.**

I. Introduction

Flapping-wing hovering flight, as performed by hummingbirds and flies, requires the wings to undergo a complicated trajectory, moving forward and backward while rotating at the correct time to optimize lift [1]. As the wings move, typically with a steep angle of attack, a vortex appears at the leading edge that adds lift [2]. During translatory motion, this vortex eventually detaches from the wing, causing a loss in lift that is known as stall. But in flapping-wing flight, the wings rotate around a vertical axis, causing the vortex to remain attached, maintaining lift [3]. The resulting unsteady, time-varying fluid flow patterns contrast with the typically steady-state flows assumed by fixed-wing aircraft and rotorcraft. To drive these motions, intricate mechanisms are required, both in biological organisms [4] and their man-made counterparts [5], [6], [7]. Flapping-wing flight therefore imposes a burden of mechanical complexity relative to fixed-wing or propellor driven craft, which has limited their application. But in return, flapping wings can produce an expanded repertoire of forces and torques for use in flight control. Theoretical studies indicate that, in addition to torques about three orthogonal axes, flapping wings can additionally produce thrusts along these axes as well [8], [9], permitting fully actuated flight motions. Flapping wings may therefore enable new types of aircraft that have an expanded flight envelope relative to existent fixed-wing vehicles and rotorcraft.

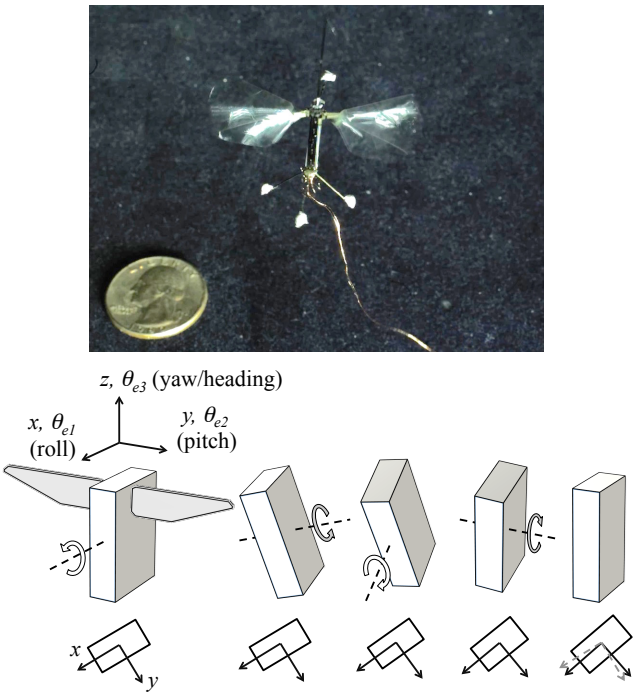

Fig. 1. A microrobotic fly such as the Harvard Robobee (top, U.S. Quarter coin shown in background for scale), or other flapping-wing or hovering flying robots may not be able to directly actuate heading or yaw angle. We propose that motion can be controlled around this axis by using cyclic body motions about other axes termed *wriggle-steering*. (middle) Illustration of sequence of motions. The body of the robot is represented as a rectangular solid, with wings shown in the leftmost image. Starting from the left, the vehicle rotates by an angle θ_{e1} around its x- or roll-axis (dashed line), then by θ_{e2} around its new (rotated) y- or pitch axis, and then reverses these two rotations about its x- and y-axes. (bottom) As shown in the projection of its base, this sequence results in a small rotation θ_{e3} around its body z- or yaw axis (the initial orientation of its axes are shown as dashed lines).

By measuring wing kinematics, studies have shown that insects employ a number of different perturbations to their baseline wing kinematics to control flight. For example, fruit flies structure their flight into bouts of forward motion punctuated by rapid yaw turns known as body saccades. The saccades are produced by a combination of changing the angle of stroke deviation as well as wing stroke amplitude [11] (For a definition of wing stroke parameters and body axis conventions, see Figures 1 and 2). Flies can also produce

*School of Engineering and Applied Sciences, Harvard University, Cambridge MA 02138 USA and the Wyss Institute for Biologically Inspired Engineering, Harvard University, Boston, MA 02115, USA, †Disney Research Pittsburgh, PA 15213 (E-mail: minster@seas.harvard.edu, peter.whitney@disneyresearch.com, rjwood@seas.harvard.edu)

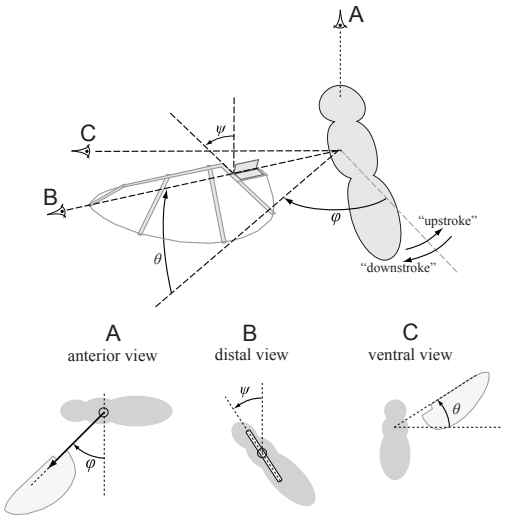

Fig. 2. Kinematic description of wing motion for hovering flapping-wing animals and robots. Definitions: φ is the wing stroke angle, θ is the stroke deviation angle, and ψ is the angle of attack. Figure used with permission from [10].

forward thrust through a "paddling" mode that consists of altering the angle of attack on the upstroke relative to the downstroke [12]. And the precise timing of angle of attack rotation at stroke reversal can alter forces as well [1].

These wing stroke strategies have inspired robotic counterparts at similar scales. As a robot's scale diminishes, machine elements such as motors, bearings, and fixed-wing airfoils become inefficient as they get smaller due to the physics of scaling: surface effects increasingly dominate Newtonian forces [13] and viscous friction increases. Thus the mechanisms in flapping-wing flight becomes more favorable than rotor-powered flight as scale diminishes. For example, the smallest robot to demonstrate controlled flight, the 80 mg RoboBee [6], is powered by a pair of flapping wings. This robot actuates its flight using independently-actuated wings: roll torque is produced by altering the amplitude of the left wing stroke relative to the right wing; pitch torque is produced by moving the mean wing stroke angle forward or backward of the center of mass (CM) [14], [6]. A larger flyer, the 19 g Nano Hummingbird, used a different approach, moving the location of a boom at the base of the wing to alter its angle of attack, thereby producing control torques about all three axes [5]. Other strategies have included moving the location of wing pivot points [15], actuating the stroke deviation angle [10], and altering the neutral angle of the flexure hinge governing the wing's neutral angle of attack [7].

As the space of design and control strategies is further explored, it may be either difficult or impossible for a given design to actuate certain degrees of freedom using available mechanisms. For example, the robotic fly presented in [14], when tethered to a sensitive torque meter, was able to produce measurable yaw or z-axis torques by driving the wings with a "split-cycle" signal. This produced wing kinematics in which the downstroke was faster or slower than the upstroke, altering the relative strength of aerodynamic drag during each of these phases, producing a net torque. However, later flight tests revealed that the magnitude of torque that could be achieved was insufficient to overcome the disturbance effects of air currents in the room and the uncertain conformation of the wire tether. Accordingly, the controller implemented in [6] was designed to be able to hover regardless of the robot's orientation and yaw angular velocity. It included a component that applied a yaw-axis torque using the split-cycle driving signal to add a damping effect to reduce yaw angular velocity, but the absolute heading or yaw angle was not regulated to a specific value. But for many reasons, it is desirable to control the heading or yaw angle of the robot. For example, landing may be facilitated by having the legs in a certain orientation, or a sensor must be aimed in a certain direction, or computational complexity of the flight controller may be reduced if the yaw rate is low.

In this work we propose a new mechanism to perform rotations about the yaw or heading angle of a hovering vehicle or animal. The basic principle is that instead of directly applying a torque about the actuated axis, the entire body of the robot is rotated by a small amount ($\ll 90°$) around the other two orthogonal axes in a cyclical fashion. The sequence of rotations is as follows: the body first rotates around its roll or x-axis by a small angle, then about its new pitch or y-axis by a similarly-sized small angle, followed by a negative x-axis roll rotation of equal magnitude, and then a negative y-axis pitch rotation. After this sequence, the body has returned to an upright orientation, but its rotation about its yaw axis has changed by a small amount (Figure 1). One can get an intuitive sense of this process in computer aided design software (CAD) by engaging the "rotate view" mode, and moving the mouse in circles on the screen: in addition to wobbling, the object in view slowly rotates around an axis intersecting near the center of the circular motions.

To our knowledge, the approach described here has not previously been proposed. A key differentiating factor is that here we rely on the ability of the body to rotate feely in space around other axes in order to perform the desired rotation. This was inspired by [16], [17] which suggested a general process for deriving trajectories for nonlinear systems with nonholonomic constraints by driving them with sinusoids. A cyclic sequence of motions is known as a Lie bracket, and can be used to drive a nonlinear system infinitesimally along a desired path. We use the term *wriggle* because of its similarity to the actuation mode of the same name proposed in that work to steer a car model.

In Section II we describe the theoretical kinematic motions of the vehicle necessary to produce the desired motion. We use a numerical model of attitude dynamics to compare yaw turning rates for different frequencies and amplitudes. In Section III we use a quasi-steady aerodynamic model of wing forces on the Robobee to simulate two proposed types of wing kinematics that could produce the necessary pitch and roll torques. The first occurs at the flapping frequency, while

the second operates at a lower frequency, producing forces on a stroke-averaged basis to produce pitch and roll torques. In Section IV, we describe the 6 degree-of-freedom (DOF) free-body model of the Robobee's body dynamics, and in Section V simulate the results of the aerodynamic torques acting on it. The results show that yaw rotation is produced as predicted. In Section VI we validate the findings with free-flight tests of a hovering Robobee, finding that the mean yaw rate closely matches the prediction of the model. We conclude with design implications for future flapping-wing robotic prototypes.

II. Kinematics model

The basic principle is purely kinematic and is illustrated in Figure 1. A series of small roll (x-axis) and pitch (y-axis) motions are made to steer motion around yaw (z-axis). Analytically, we can describe the result of a single cycle using a rotation matrix $\boldsymbol{R} \in \mathbb{R}^{3\times 3}$ to represent orientation. For a vector $\boldsymbol{v}'$ given in body-attached coordinates, $\boldsymbol{v} = \boldsymbol{R}\boldsymbol{v}'$ is the vector given in world coordinates. For infinitesimal rotations ϵ_1 and ϵ_2 around x and y axes, respectively, the result is $\boldsymbol{R} = \begin{bmatrix} 1 & -\epsilon_1\epsilon_2 & 0 \\ \epsilon_1\epsilon_2 & 1 & 0 \\ 0 & 0 & 1 \end{bmatrix}$, neglecting higher-order terms (computed using axis-angle rotations in python's `sympy` package).

A more realistic scenario requires that these motions be smooth, minimizing the magnitude of required torques. This suggests sinusoidal oscillations [16]. These can be driven with a sinusoidal torque

$$\boldsymbol{\tau}_c = T_0 \begin{bmatrix} \sin(2\pi F t) \\ \sin(2\pi F t + \delta) \\ 0 \end{bmatrix}, \tag{1}$$

where T_0 is the torque oscillation amplitude, which must be less than or equal to the maximum possible torque that can be achieved by the vehicle's wings. The quantity F is the frequency of the driving oscillations, t is time, and δ is the phase offset. Note that the torque about the z-axis is zero.

To understand how these torques map to body motions, consider a dynamic model of the attitude dynamics of a flapping-wing flyer, parameterized by Euler Angles. The attitude is represented by an array of three angles $\boldsymbol{\theta}_e \in \mathbb{R}^3$ and is obtained by first rotating by an angle θ_{e3} (yaw) around the body z-axis, then by θ_{e2} (pitch) around the new body y-axis, and then by θ_{e1} (roll) around the new body x-axis. This representation has singularities at extreme attitudes but is convenient to represent motion in the neighborhood of a certain attitude. Its dynamics can be written as

$$\dot{\boldsymbol{\theta}}_e = \mathbf{W}(\boldsymbol{\theta}_e)\,\boldsymbol{\omega}, \tag{2}$$

$$\mathbb{J}\,\dot{\boldsymbol{\omega}} = \boldsymbol{\tau} - \boldsymbol{\omega} \times \mathbb{J}\,\boldsymbol{\omega}, \tag{3}$$

where $\boldsymbol{\omega} \in \mathbb{R}^3$ is the angular velocity vector, $\boldsymbol{\tau} \in \mathbb{R}^3$ is a torque applied to the body by aerodynamic forces and control torques generated by the wings, and $\mathbb{J} \in \mathbb{R}^{3\times 3}$ is the matrix of the mass moment of inertia given in body-attached coordinates. The quantity $\mathbf{W}(\boldsymbol{\theta}_e)$ is a matrix that relates the angular velocity $\boldsymbol{\omega}$ to the rate of change in Euler Angles. Rewriting equation (2) in terms of these coordinates gives

$$\begin{bmatrix} \dot{\theta}_{e1} \\ \dot{\theta}_{e2} \\ \dot{\theta}_{e3} \end{bmatrix} = \begin{bmatrix} 1 & \sin\theta_{e1}\tan\theta_{e2} & \cos\theta_{e1}\tan\theta_{e2} \\ 0 & \cos\theta_{e1} & -\sin\theta_{e1} \\ 0 & \sin\theta_{e1}/\cos\theta_{e2} & \cos\theta_{e1}/\cos\theta_{e2} \end{bmatrix} \begin{bmatrix} \omega_1 \\ \omega_2 \\ \omega_3 \end{bmatrix}. \tag{4}$$

The kinematic behavior can be understood using a simplification in which the inertia matrix is identity, $\mathbb{J} = \mathbf{I}$, so that the term $\boldsymbol{\omega} \times \mathbb{J}\,\boldsymbol{\omega} = \boldsymbol{\omega} \times (\mathbf{I}\boldsymbol{\omega}) = \boldsymbol{\omega} \times \boldsymbol{\omega} = \mathbf{0}$. Then Equation (3) reduces to $\dot{\boldsymbol{\omega}} = \boldsymbol{\tau}$, and for zero initial conditions gives

$$\boldsymbol{\omega} = \frac{T_0}{2\pi F} \begin{bmatrix} \cos(2\pi F t) \\ \cos(2\pi F t + \delta) \\ 0 \end{bmatrix}. \tag{5}$$

We analyze the resulting motion by numerically integrating Equations (4) and (5) with a fixed-step time increment of 0.1 ms with a $\delta = 90^{\text{o}}$ phase offset between ω_1 and ω_2. Figure 3 (and video) shows the results of simulations. Oscillating $\boldsymbol{\omega}$ inputs cause the two Euler Angles θ_{e1} and θ_{e2} to oscillate cyclically around a mean value of zero so that the body remains upright. Results show that a), for a given amplitude of oscillations in θ_{e1} and θ_{e2}, a higher frequency results in a higher cycle-averaged rate of yaw rotation, $\dot{\theta}_{e3}$, b) for a constant amplitude of $\boldsymbol{\omega}$ oscillations ($= T_0/2\pi F$ in Equation (5)), the amplitude in oscillations of θ_{e1} and θ_{e2} increases, resulting in larger $\dot{\theta}_{e3}$, and c) that $\dot{\theta}_{e3}$ can be varied by varying the magnitude of the oscillations about one of the two axes. The simulation also confirmed (data not shown) that $\dot{\theta}_{e3}$ is highest for $\delta = 90°$, falling to zero at $\delta = 0°$ and $\delta = 180°$ (in the latter two cases, θ_{e3} varies in time, but its stroke-averaged value and time-derivative remain zero).

III. Aerodynamics model and simulations

With a demonstration of the operation of the basic kinematics, we now turn to how to generate the required torques about the pitch and roll axes by altering wing motions relative to baseline hovering kinematics.

1) Oscillating at the flapping frequency: At the flapping frequency, note that the flapping wings themselves produce an oscillating pitch torque. This is because drag produced by their forward-backward motion acts at a distance above the center of mass (CM). The free-body dynamics simulations described below suggest the amplitude of θ_{e2} oscillations is about $1°$ for the robot fly considered here. The flapping frequency of this vehicle is 120 Hz, which is far below its ~3 Hz unstable natural mode predicted for body oscillations [18], suggesting that wing motion should not excite its natural mode.

To achieve wriggling, roll oscillations must occur at about a $90°$ phase difference relative to pitch oscillations. Because basic aerodynamics suggest that lift and drag typically occur in phase with one another for forward motion, we instead consider incorporating vertical (z-axis) motion into the wing kinematics. Previously, a mechanism was proposed and demonstrated that could actuate the stroke deviation angle

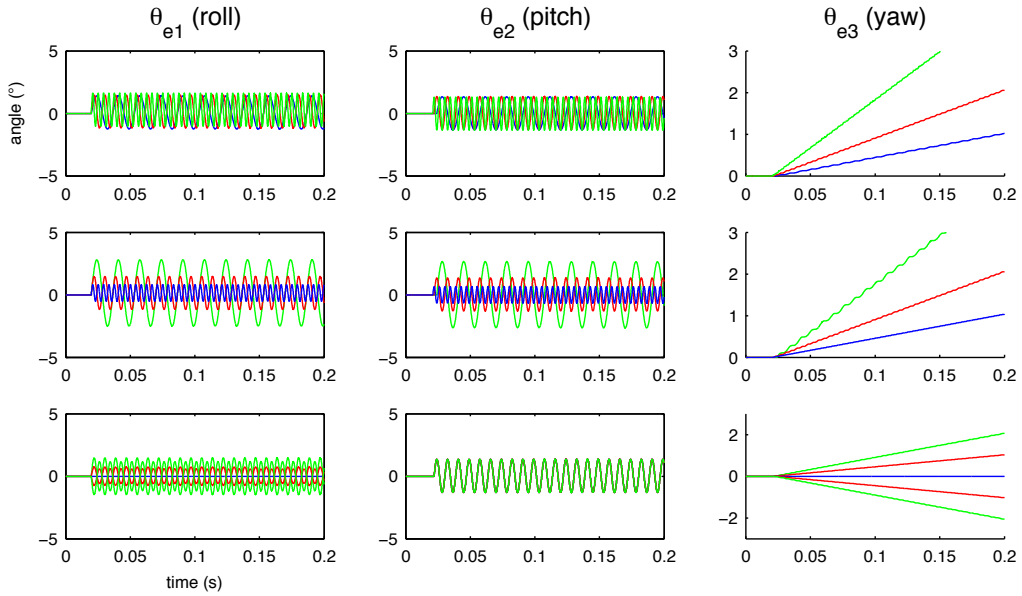

Fig. 3. Kinematics of wriggle-steering. Motions of the body attitude Euler Angles $\boldsymbol{\theta}_e$ were computed from a numerical simulation of Equation (4) driven by the sinusoid input in $\boldsymbol{\omega}$ given by Equation (5). In all cases, pitch and roll oscillations are offset by $\delta = 90°$ phase. (top) If the amplitude of body rotations θ_{e1} and θ_{e2} are held constant, a higher oscillation frequency F in $\boldsymbol{\omega}$ results in a higher cycle-averaged rate of change in yaw angle, $\dot{\theta}_{e3}$. Examples are plotted for frequencies F of 60 Hz (blue), 120 Hz (red), and 240 Hz (green). (middle) For oscillations with a fixed torque amplitude T_0 (Equation (1)), corresponding to a fixed amplitude in body angular velocity $\boldsymbol{\omega}$ oscillations (Equation (5)), lower frequency results in a larger amplitude oscillations in θ_{e1} and θ_{e2}, resulting in a higher $\dot{\theta}_{e3}$. Examples are plotted for oscillations with $\boldsymbol{\omega}$ amplitude of 1000°/sec for frequencies F of 60 Hz (green), 120 Hz (red), and 240 Hz (blue). (bottom) Given a constant pitch oscillation angle amplitude, yaw rate can be varied by modulating the magnitude of roll oscillations. Examples are plotted for a pitch amplitude of 1000°/s, and roll amplitudes of 1000°/s, 500°/s, and 0°/s.

θ of a microrobotic fly, in addition to the necessary stroke angle, by adding an extra piezo actuator [10]. Figure 4 shows the resulting wing kinematic perturbation: the stroke plane angle θ oscillates at the same frequency as wing flapping so that the wings move up and down as they move front to back. In [10], the oval stroke pattern was found to be energetically less efficient at generating lift than other wing kinematics, but we note here that it is ideal for producing wriggling because the resulting vertical wing motion produces roll torques out of phase with stroke-induced pitch torques.

2) Quasi-steady aerodynamics simulation: To demonstrate the ability to produce the necessary actuation mode, the proposed driving wing kinematics were simulated in a quasi-steady aerodynamic model that includes passive flexion of the elastic flexure around which the wing's angle of attack is allowed to rotate during wing motions [19]. This model, which estimates resulting forces and torques, was validated on experimental force data taken from flapping wings, and is based on the characteristics of the wing and hinge of the vehicle in [6]. Figures 5 and 6 show the resulting body torques arising out of the "flat" and "oval" kinematics, respectively. The torque produced by "oval" kinematics has a fundamental harmonic in roll torque that is 90º out of phase from pitch torque, as desired. The magnitude of the roll torque can be altered by varying the size of the stroke angle deviation, providing a means for varying $\dot{\theta}_{e3}$.

3) Oscillating below flapping frequency: We now consider oscillations driven at lower frequency, driven by torques that

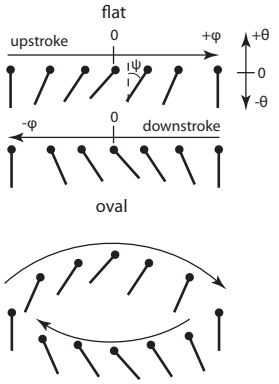

Fig. 4. Proposed wing kinematics that generate a profile of roll torques necessary to induce wriggling at the flapping frequency. An "unwrapped" distal viewpoint from the tip of the wing (As in Figure 2B) shows lines that represent the angle of attack of the wing, with a dot denoting the leading edge. In the baseline "flat" kinematics (top), the leading edge of the wings remains in a plane, so that the stroke deviation angle θ remains a constant zero. With "oval" kinematics (bottom), the stroke deviation angle varies up and down at the same frequency as the flapping frequency. The up-and-down motion adds a net roll torque, particularly around the moment of stroke reversal. Figure used with permission from [10].

are produced on a stroke-averaged basis. The robot shown in Figure 1 has a pair of independently-actuated wings that can produce orthogonal stroke-averaged pitch and roll torques. Following [6], which used the simulation derived in [19], we derive a simplified numerical linearization to provide a

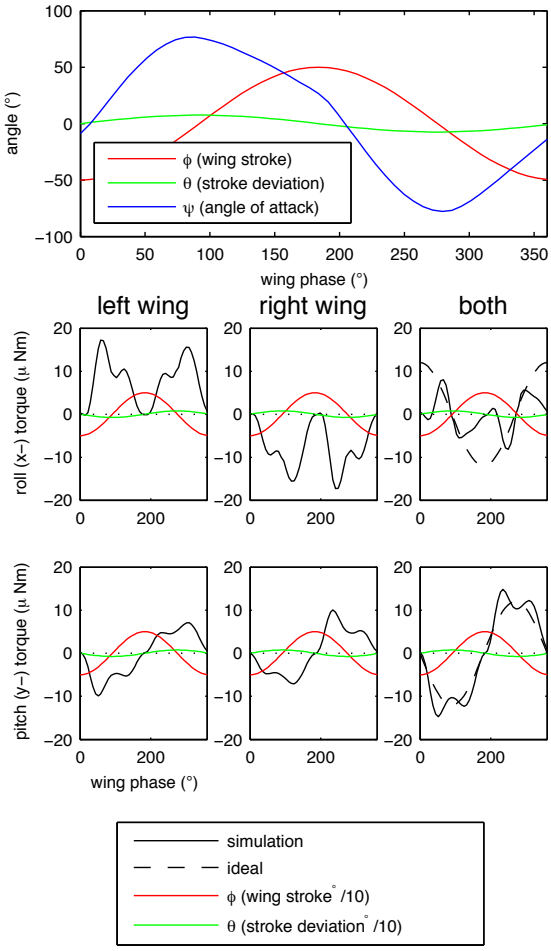

Fig. 5. Wing kinematics (top) and resulting torques (bottom) for the "oval" trajectory in shown in Figure 4. The amplitude of stroke deviation θ is 7.5º (15º peak-to-peak). The resulting torque from the wings (black, solid line) is compared against the ideal (black, dashed line) given by Equation (1). Large deviations from the ideal roll torque profile at phases of 0° and 180° occur at time points when the angle of attack of the wing, ψ, is near zero, that is, when it is near vertical. At these phases, the cross-sectional area exposed to the flow is very small, leading to small forces and therefore torque during the wing's predominantly z-axis motions at that time. Nevertheless, this wing motion produces a fundamental harmonic in roll torque at the desired 90° phase shift relative to pitch torque.

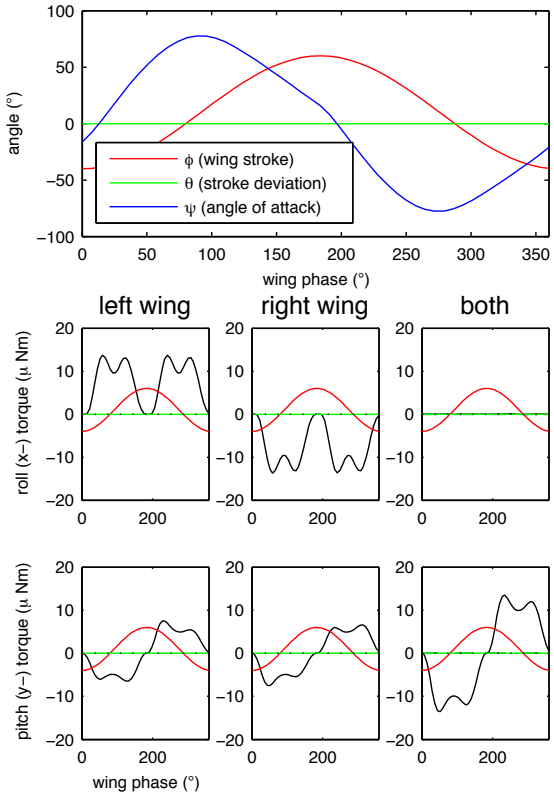

Fig. 6. Wing kinematics (top) and resulting torques (bottom) for the "flat" trajectory shown in Figure 4, in which stroke deviation remains at $\theta = 0$. No net roll torque arises.

mapping between desired torques and the necessary wing kinematics to produce them. Given stroke kinematics in which Φ is the amplitude of wing stroke cycles $\varphi(t)$, Φ_Δ is the difference in wing stroke amplitude between left and right wings, and Φ_m is the shift forward or backward in mean wing stroke angle, then the lift force f_l and control torques τ_{c1} and τ_{c2} follow the following relation to first order:

$$\begin{aligned} f_l &= \alpha_l \Phi - \beta_l \\ \tau_{c1} &= (\alpha_1 \Phi - \beta_1)\Phi_\Delta \\ \tau_{c2} &= (\alpha_2 \Phi - \beta_2)\Phi_m. \end{aligned} \tag{6}$$

The α and β quantities are constants derived from numerical linearization. The control signal Φ_Δ produces a roll torque by changing the relative amplitudes of the left and right wing strokes, producing a differential lift force. Changing Φ_m produces a pitch torque by moving the "mean wing stroke angle"–the time-averaged angle of the forward-backward motion of the wings–in front ($+x$) or behind ($-x$) the CM [14]. These two torques are approximately orthogonal, so they can be considered independently. The torque magnitudes, however, are dependent on the wing stroke amplitude Φ. A second-order linear model of the piezo-transmission-wing resonant system is used to map these wing stroke kinematics to electrical driving signals to the piezo actuators [20].

IV. Free-body simulation of robot dynamics

To provide a more realistic test of wriggle-steering, we simulated forces and torques on a 6DOF dynamic simulation of the flapping-wing vehicle described in [6]. The model includes a stroke-averaged model of aerodynamic drag on the wings, so it additionally incorporates velocity in the robot's state according to

$$m\,\dot{\boldsymbol{v}} = \boldsymbol{f} - \boldsymbol{\omega} \times m\,\boldsymbol{v}. \tag{7}$$

In this equation, $\boldsymbol{v} \in \mathbb{R}^3$ is the velocity of the CM, $\boldsymbol{f} \in \mathbb{R}^3$ are external forces acting on the CM, and m is the mass of the vehicle. The stroke-averaged aerodynamic drag is

$$\boldsymbol{f}_d = -b_w \boldsymbol{v}_w = -b_w(\boldsymbol{v} + \boldsymbol{\omega} \times \boldsymbol{r}_w), \tag{8}$$

quantity	symbol	quantity	units
mass	m	81×10^{-6}	kg
moment of inertia (x-axis)	J_1	1.42×10^{-9}	kg m^2
moment of inertia (y-axis)	J_2	1.34×10^{-9}	kg m^2
moment of inertia (z-axis)	J_3	0.45×10^{-9}	kg m^2
vector, CM to wing pair midpoint	$\boldsymbol{r}_w$	$\begin{bmatrix} 0 \\ 0 \\ 7 \times 10^{-3} \end{bmatrix}$	m
aerodynamic drag constant	b_w	2×10^{-4}	Nsm^{-1}

TABLE I

ESTIMATED PARAMETERS FOR THE ROBOTIC VEHICLE USED IN SIMULATIONS.

where b_w is the air drag proportionality constant, and $\boldsymbol{v}_w = \boldsymbol{\omega} \times \boldsymbol{r}_w$ is the velocity of the point on the body midway between the wings [18].

Parameters for the robotic fly in this simulation are given in Table I and were derived from computer aided design (CAD) software [6], a precision scale, and wind tunnel tests [18] on the Robobee. The dynamics of the simulation reproduce the robot's dynamics, including dynamic instability in flight, so an additional feedback torque was added to the simulation, $\boldsymbol{\tau}_c = -k_d \boldsymbol{\omega}$, with a gain of $k_d = 1.5 \times 10^{-7}$ Nms/rad, so that the simulated robot remains upright in flight [18].

A. Oscillations driven at stroke-frequency

The results of the simulation of the robot fly (Equations (2)–(4), (7), and (8)) driven by torques plotted in Figure 5, show that torques produced by oval wing kinematics can produce yaw rotations, with a rate proportional to the magnitude of stroke plane deviations θ (Figure 7). We note that the torques estimated by the quasi-steady aerodynamic simulation assumed the vehicle was still and in quiescent flow, but this assumption may not necessarily hold under conditions in which the vehicle is in motion. However, the amplitude of pitch and roll oscillations are small, only 1-2º, suggesting that they may have a small effect on the simulated aerodynamics, and lateral motions are near zero.

B. Oscillations below the flapping frequency

In this simulation of the robotic fly (also given by Equations (2)–(4), (7), and (8)), driven by stroke-averaged torques, the torque amplitude T_0 was set to 0.5 μNm, approximately half of the maximum torque that the robot's wings have been able to produce along its pitch and roll axes [14]. The results for driving frequencies of $F = 5,\ 10,$ and 20 Hz, are shown in Figure 8. As in Figure 3, we found that driving torques with the same amplitude but lower frequency results in larger deviations in attitude, and results in a larger cycle-averaged yaw angular rate $\dot{\theta}_{e3}$.

V. FLIGHT TESTS OF LOW-FREQUENCY OSCILLATIONS

We verified that the simulations described above could operate as desired by performing flight tests on a hovering robotic fly (Figure 1). Robot power and control commands were sent through a lightweight compliant tether cable

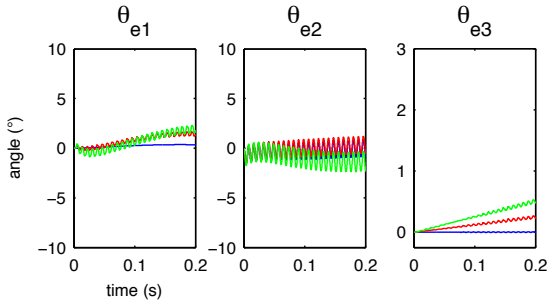

Fig. 7. Free-body simulation of the robotic fly subject to wriggling driven at the flapping frequency. Wing-induced torques were estimated from a quasi-steady model of flapping-wing aerodynamics (Figure 5). Pitch oscillations about θ_{e2} are driven by the forward-backward motion of the flapping wings while roll oscillations about θ_{e1} are driven by an "oval" stroke deviation pattern shown in Figure 4. Deviation amplitudes are 0° (blue), 7.5° (red), and 15º (green). A larger stroke deviation produces a larger roll torque and a correspondingly larger stroke-averaged yaw-rate $\dot{\theta}_{e3}$ (right). The slow transients are the result the perturbation when the wings first start moving, but have a small effect on yaw rotations.

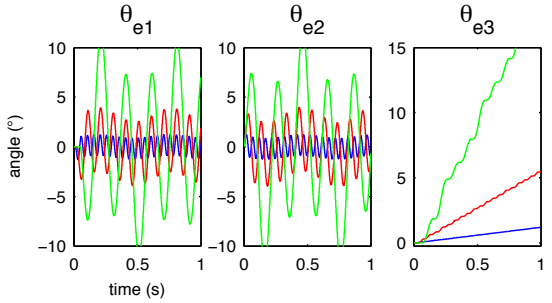

Fig. 8. Simulation of the free-body motion of of the robotic fly subject to wriggling driven below the flapping frequency by *stroke-averaged* torques. Wing-induced torques were estimated from a quasi-steady model of stroke-averaged flapping-wing aerodynamics (Equation (6)). The driving signal is given by Equation (1), with oscillations driven at frequencies of $F = 5$ Hz (green), 10 Hz (red), and and 20 Hz (blue). A lower driving frequency results in larger attitude oscillations in θ_{e2} and θ_{e2}, resulting in a larger cycle-averaged yaw angular rate $\dot{\theta}_{e3}$ (right).

consisting of four 51-gauge (0.022 mm diameter) copper wires [6]. We performed flights tests in a motion capture arena with an array of calibrated cameras (Vicon T040-series, Oxford, UK). Each camera emits bright infrared light that is reflected from a number of retroreflective markers mounted on the vehicle so that its position and orientation can be reconstructed in real-time for later analysis. In all flights, computations to generate signals for the piezoelectric actuators to drive wing motion, as well as to map desired control torques to these signals, were performed on an XPC Target, a desktop computer running a real-time operating system (Mathworks, Natick, MA USA). Analog voltage outputs from an analog-to-digital conversion board (National Instruments, Austin TX USA, model PCI-6259) installed in this computer were amplified by high-voltage piezo amplifiers and transmitted to the robotic fly through the tether cable.

In these flight tests, we introduced a three-filament kevlar restraining thread at the top of the robot to reduce wear on the wing hinges during crash landings. This was inspired by

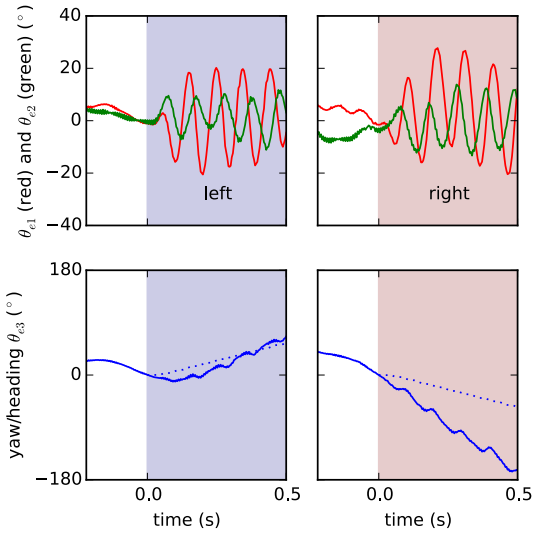

Fig. 9. Example of wriggle-induced left (left) and right (right) turn during hover of fly-sized flapping-wing robot. (top) Euler Angles θ_{e1} (roll rotation, red) and θ_{e2} (pitch rotation, green) do not oscillate before turn, but oscillate due to commanded inputs during turning phase. Roll oscillations either lead (left turn) or lag (right turn) pitch oscillations by 90°, resulting in a turn of the desired polarity. Roll oscillations are larger than pitch oscillations because of a resonant mode in the feedback system near the commanded oscillation frequency. (bottom) The heading or yaw angle θ_{e3} changes during the turning phase. Dashed line shows the prediction of the model for a pitch oscillation amplitude of 10° and a roll oscillation amplitude of 20°.

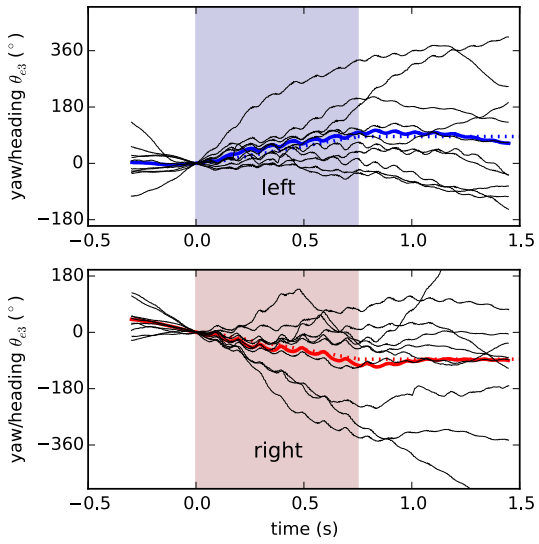

Fig. 10. Flight tests of wriggle-induced turns from 24 separate events. (top) The mean of the 12 turn events (black) is shown as a thick blue line, and the prediction of the model shown as a dashed line, showing a close match. (bottom) Equivalent plot for 12 right turns. Disturbances from the tether are occasionally sufficiently large to overcome the effect of the wriggle-turns.

the umbilical cord used to stop the fall of walking robots in the event of malfunction [21]. In both cases, the thread mass is negligible relative to the robot – each 30 cm filament has a mass of 60 μg, measured on a precision scale, giving the bundle of three a mass of approximately 0.2 mg, less than 0.2% of the total robot mass. To test its compliance, we extended a single filament horizontally 10 cm. The length of thread was unable to support its own 20 μg weight, indicating that the torque that a three-filament bundle can apply to the robot is less than $3 \cdot 20 \times 10^{-9}[\text{kg}] \cdot 9.81 \left[\frac{\text{N}}{\text{kg}}\right] \cdot 0.01[\text{m}] \approx 0.02$ μNm, which is small relative to control torques, calculated to have a root mean square (RMS) magnitude of 0.35 μNm for pitch and roll during normal hovering flights.

Flight tests consisted of a takeoff and a short period of hover (4 seconds) to stabilize the dynamics and allow the adaptive controller to tune its parameters (roll and pitch trim torques and three orthogonal force trim values). The controller was functionally similar to [6], and consists of an inner loop controlling the attitude (roll and pitch angles) of the robot and an outer loop that regulates position by commanding attitude changes to the inner loop. To produce the wriggling oscillations, an oscillating setpoint attitude was sent to the attitude feedback controller to command pitch and roll oscillations with an amplitude of 10° at a frequency $F = 10$ Hz. Larger amplitudes are in principle possible, but cause undesirable larger position errors.

Figure 9 shows that the flight controller was successfully able to induce roll oscillations that either led or lagged pitch oscillations by 90°. This resulted in either a left or a right turn, respectively (video shows these two turns).

Figure 10 shows data from 24 separate turn events, 12 in each direction, resulting in turns of the desired polarity. The mean angular velocity of the robot was approximately 131°/sec in leftward direction and -139°/sec in the rightward direction. The prediction of the model, for a pitch oscillation amplitude of 10° and a roll oscillation amplitude of 20°, closely follows the behavior of the robot, with 12% and 18% error for left and right turns, respectively. However, the robot's turn rate was variable, occasionally even going in the opposite direction of the wriggle-steering. This indicates that disturbances, likely primarily due to the wire tether, are larger than is possible to consistently overcome using wriggle steering to control yaw angle.

VI. Conclusions

This paper describes a method to rotate the yaw or heading angle of underactuated flapping-wing hovering flying robots and animals. Termed *wriggle-steering*, it consists of driving vehicle rotations around a certain axis by cyclically rotating by small angles about two other axes. This was motivated by a deficiency in an existing design of a fly-sized hovering robot, which is unable to reliably regulate its heading to a desired value using known wing kinematics. To the authors' knowledge, inducing motion by wriggle-steering way has not previously been proposed.

We used a simplified kinematic analysis to maximize yaw angular rate under the realistic situation that actuation authority T_0 (maximum achievable pitch and roll torque)

is limited. Our results indicate that this can be achieved by minimizing oscillation cycle frequency. The lower frequency produces higher-amplitude rotation cycles. However, large oscillations may produce undesirable consequences. As amplitude increases, the cycle-averaged lift force decreases because more of the thrust from the wings is directed laterally. Oscillations also may make it more difficult to collect feedback from onboard sensors, as well as making the vehicle's aerodynamics harder to predict. These consequences must be weighed against design objectives.

We then proposed two mechanisms by which a flapping-wing flying robot could perform the desired motion. The first consists of wriggling at the stroke frequency. As a conceptual exercise, this is appealing because it relies on body pitching oscillations that already occur as a result of the robot being driven by flapping wings. But it requires additional actuators in the robot design, and our quasi-steady aerodynamic simulations and free-body model suggest it produces a low yaw rotation rate of 2.5°/s, limiting its applicability. The second consists of lower-frequency wriggling, driven by stroke-averaged torques. This produced much higher turn rates in simulation, and can be performed on a currently-available robotic fly design. We performed hovering flight tests showed that the robot's average yaw rate was comparable to the prediction of the model in both directions.

Although our tests indicated that wriggle-steering could not consistently overcome tether disturbances acting on our robotic vehicle, our purpose in this work was merely to introduce an actuation mode that could in principle perform the desired motion in underactuated designs. Our flight tests provide encouraging evidence that wriggle-steering operates as desired, reducing the need for additional actuators to simplify design and reduce weight. In the future, consistent control of heading angle may be facilitated as follows. First, disturbances could be reduced by using even thinner tether wire, or better, removing it entirely by using batteries. Alternatively, wriggling could be combined with split-cycle signals to the actuators [14] to provide greater control authority. Combining actuation modes like this appears to be a common approach used in biology. For example, sudden heading changes in flies in flight, termed body-saccades, are driven by changes both in stroke deviation and amplitude [11].

We conclude by remarking that wriggle-steering as proposed here could be performed by other, non-hovering types of robotic aerial vehicles. It is, however, impractical on manned vehicles because rapid cyclic oscillations could lead to pilot discomfort. But for a robotic aerial vehicle, as long as the rotation angle along any two axes can be actuated, then the third can rotated by an equivalent style of phased cyclic excitations.

VII. Acknowledgements

The authors would like to thank Richard M. Murray, Ben Finio, and Pakpong Chirarattananon for insightful discussions. This work was partially supported by the National Science Foundation (award numbers CCF-0926148) and the Wyss Institute for Biologically Inspired Engineering. Any opinions, findings, and conclusions or recommendations expressed in this material are those of the authors and do not necessarily reflect the views of the National Science Foundation.

References

[1] Michael H. Dickinson, Fritz-Olaf Lehmann, and Sanjay P. Sane. Wing rotation and the aerodynamic basis of insect flight. *Science*, 204:1954–1960, 1999.

[2] M. H. Dickinson and K. G. Gotz. Unsteady aerodynamic performance of model wings at low reynolds numbers. *The Journal of Experimental Biology*, 174(1):45–64, 1993.

[3] Charles P. Ellington, Coen van den Berg, Alexander P. Willmott, and Adrian L. R. Thomas. Leading-edge vortices in insect flight. *Nature*, 384(19):626–630, December 1996.

[4] Michael H. Dickinson and Michael S. Tu. The function of the dipteran flight muscle. *Journal of Comparative Physiology A*, 116A:230–238, 1997.

[5] Matthew Keennon, Karl Klingebiel, Henry Won, and Alexander Andriukov. Development of the nano hummingbird: A tailless flapping wing micro air vehicle. In *AIAA Aerospace Sciences Meeting*, pages 1–24, Reston, VA, 9–12 January 2012. AIAA.

[6] Kevin Y. Ma, Pakpong Chirarattananon, Sawyer B. Fuller, and Robert Wood. Controlled flight of a biologically inspired, insect-scale robot. *Science*, 340(6132):603–607, 2013.

[7] Zhi Ern Teoh and Robert J. Wood. A flapping-wing microrobot with a differential angle-of-attack mechanism. In *Robotics and Automation (ICRA), 2013 IEEE Int. Conf.*, 2013.

[8] Jiang-hao Wu and Mao Sun. Control of flight forces and moments by flapping wings of model bumblebee. *Applied Mathematics and Mechanics*, 29(3):333–350, 2008.

[9] Michael W Oppenheimer, Isaac E Weintraub, David O Sigthorsson, and David B Doman. Control of a minimally actuated biomimetic vehicle using quarter-cycle wingbeat modulation. *Journal of Guidance, Control, and Dynamics*, pages 1–10, 2015.

[10] B.M. Finio, J.P. Whitney, and R.J. Wood. Stroke plane deviation for a microrobotic fly. In *Intelligent Robots and Systems (IROS), 2010 IEEE/RSJ Int. Conf.*, pages 3378 –3385, 2010.

[11] Steven N. Fry, Rosalyn Sayaman, and Michael H. Dickinson. The aerodynamics of free-flight maneuvers in *Drosophila*. *Science*, 300:495–498, 2003.

[12] Leif Ristroph, Attila J Bergou, John Guckenheimer, Z. Jane Wang, and Itai Cohen. Paddling mode of forward flight in insects. *Phys Rev Lett*, 106(17):178103, Apr 2011.

[13] W. S. N. Trimmer. Microbots and micromechanical systems. *Sensors and Actuators*, 19:267–287, 1989.

[14] Kevin Y. Ma, Samuel M. Felton, and Robert J. Wood. Design, fabrication, and modeling of the split actuator microrobotic bee. In *Robotics and Automation (ICRA), 2012 IEEE Int. Conf.*, pages 1133–1140, St. Paul, MN, 14–18 May 2012.

[15] M Karásek, A Hua, Y Nan, M Lalami, and A Preumont. Pitch and roll control mechanism for a hovering flapping wing mav. In *Micro Air Vehicles (IMAV), 2014 Int. Conf. and Competition*, 2014.

[16] Richard M. Murray and S. Shankar Sastry. Nonholonomic motion planning: Steering using sinusoids. *IEEE Trans. on Automatic Control*, 38(5):700–716, May 1993.

[17] Richard M. Murray. Geometric phases, control theory, and robotics. In *Proceedings of the Board on Mathematical Sciences, Science and Technology Symposium*, Washington, DC, 1994.

[18] Sawyer B. Fuller, Michael Karpelson, Andrea Censi, Kevin Y. Ma, and Robert J. Wood. Controlling free flight of a robotic fly using an onboard vision sensor inspired by insect ocelli. *J. Royal Society Interface*, 11(97), August 2014.

[19] JP Whitney and RJ Wood. Aeromechanics of passive rotation in flapping flight. *J. Fluid Mechanics*, 660(1):197–220, 2010.

[20] Ben M. Finio, Nestor O. Perez-Arancibia, and Robert J. Wood. System identification and linear time-invariant modeling of an insect-sized flapping-wing micro air vehicle. In *Intelligent Robots and Systems (IROS), 2011 IEEE/RSJ Int. Conf.*, September 2011.

[21] Marc H. Raibert. *Legged robots that balance*. MIT press, 1986.